Inorganic Chemistry

pubs.acs.org/IC

Article

On the Demise of PPP-Ligated Iron Catalysts in the Formic Acid Dehydrogenation Reaction

Bedraj Pandey, Jeanette A. Krause, and Hairong Guan*

Cite This: *Inorg. Chem.* 2023, 62, 18714−18723

Read Online

ACCESS | Metrics & More | Article Recommendations | Supporting Information

ABSTRACT: The PPP-ligated iron complexes, *cis*-($^{i\mathrm{Pr}}$PP$^{\mathrm{R}}$P)-FeH$_2$(CO) [$^{i\mathrm{Pr}}$PP$^{\mathrm{R}}$P = (*o*-^{i}Pr$_2$PC$_6$H$_4$)$_2$PR (R = H or Me)], catalyze the dehydrogenation of formic acid to carbon dioxide but lose their catalytic activity over time. This study focuses on the analysis of the species formed from the degradation of *cis*-($^{i\mathrm{Pr}}$PP$^{\mathrm{Me}}$P)FeH$_2$(CO) over its course of catalyzing the dehydrogenation reaction. These degradation products include species both soluble and insoluble in the reaction medium. The soluble component of the decomposed catalyst is a mixture of *cis*-[($^{i\mathrm{Pr}}$PP$^{\mathrm{Me}}$P)FeH(CO)$_2$][(HCO$_2$)-(HCO$_2$H)$_x$], protonated $^{i\mathrm{Pr}}$PP$^{\mathrm{Me}}$P, and oxidation products resulting from adventitious O$_2$. The precipitate is solvated Fe(OCHO)$_2$. Further mechanistic investigation suggests that *cis*-[($^{i\mathrm{Pr}}$PP$^{\mathrm{Me}}$P)FeH(CO)$_2$][(HCO$_2$)(HCO$_2$H)$_x$] displays diminished but measurable catalytic activity, likely through the displacement of a CO ligand by the formate ion. The formation of Fe(OCHO)$_2$ along with the dissociation of $^{i\mathrm{Pr}}$PP$^{\mathrm{Me}}$P is responsible for the eventual loss of catalytic activity.

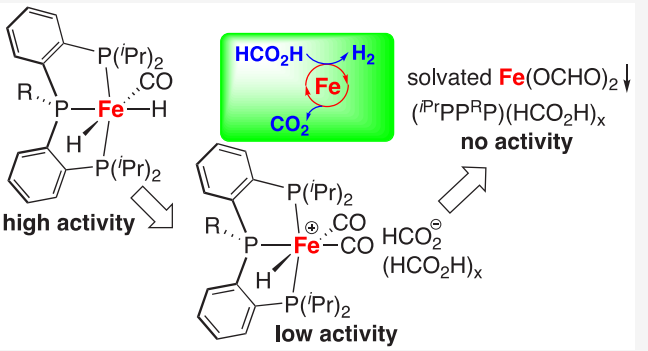

INTRODUCTION

Transition-metal-catalyzed reactions that proceed in an acidic medium or produce Brønsted acids pose significant challenges for catalyst design. The supporting ligands, especially nitrogen- and phosphorus-based ligands, could be protonated to trigger catalyst degradation. This problem is expected to be more pronounced with 3d metal systems in which the metal−ligand bonds are more polarized or ionic.[1] Nevertheless, acid-tolerant homogeneous catalysts are known in the literature; notable examples include [{Cp*Ru(CO)$_2$}$_2$(μ-H)]OTf for catalytic deoxygenation of diols assisted by triflic acid[2] and triphos-ligated cobalt complexes [triphos = (Ph$_2$PCH$_2$)$_3$CCH$_3$] for catalytic hydrogenation of carboxylic acids.[3]

One of the reactions involving acids is the catalytic dehydrogenation of formic acid to H$_2$ and CO$_2$, which has been studied extensively in recent years.[4] The growing interest in this research area stems from the promise of using formic acid as an H$_2$ energy carrier.[5] Among the metals that can be used to promote this specific transformation, iron is particularly attractive due to its high terrestrial abundance. Early studies of iron catalysts for formic acid dehydrogenation relied on simple salts such as FeCl$_2$ and FeCl$_3$[6] or a mixture of Fe$_3$(CO)$_{12}$, terpyridine, and a monophosphine ligand.[7] More recent catalyst design has been focused on well-defined iron complexes supported by a phosphorus-based, tridentate/pincer,[8] or tetradentate[9] ligand. Of particular note is ($^{i\mathrm{Pr}}$PN$^{\mathrm{H}}$P)FeH(CO)-(OCHO) [$^{i\mathrm{Pr}}$PN$^{\mathrm{H}}$P = (^{i}Pr$_2$PCH$_2$CH$_2$)$_2$NH (see Chart 1 for the structure)] developed by Bernskoetter, Hazari, and Schneider, which catalyzes the release of H$_2$ from formic acid with turnover

Chart 1. Selected Iron Pincer Complexes for Catalytic Dehydrogenation of Formic Acid

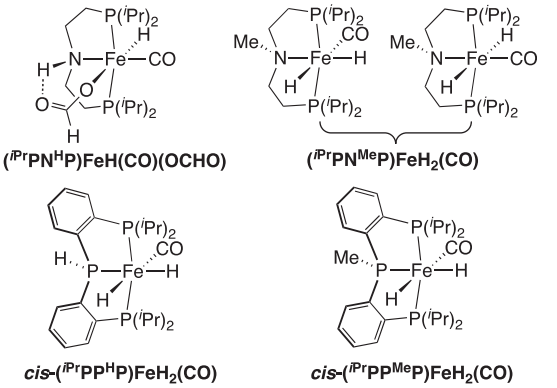

Received: September 6, 2023
Revised: October 6, 2023
Accepted: October 13, 2023
Published: October 31, 2023

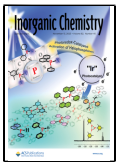

numbers (TONs) as high as 983 642.[8b] Despite the progress made, most of these catalytic systems require a base additive[8a,c,d] or a ligand:metal ratio higher than what is suggested by the proposed catalyst structure.[9] Ideally, the catalytic dehydrogenation reaction should be performed in neat formic acid without any additive to maximize the volumetric and gravimetric capacity of hydrogen (up to 53 g/L and 4.4 wt %, respectively), which currently is more realistic with iridium- or ruthenium-based catalysts.[10,11]

The precise function of the base additive, excess ligand, and dilution with a solvent in formic acid dehydrogenation is not fully understood and may vary with the different catalytic systems. The shared consequence is the attenuated acidity that may help extend the life span of the catalysts. To develop more efficient and robust systems, it is critical to understand how iron complexes degrade during the catalytic process. To this end, Hazari and co-workers have examined the stability of several catalytically relevant species, including $[(^{i\mathrm{Pr}}\mathrm{PN^HP})\mathrm{FeH(CO)(THF)}]^+$ and $(^{i\mathrm{Pr}}\mathrm{PN^HP})\mathrm{FeH(CO)(PF_6)}$, which, in the absence of formic acid, decompose to $[(^{i\mathrm{Pr}}\mathrm{PN^HP})\mathrm{FeH(CO)_2}]^+$, $^{i\mathrm{Pr}}\mathrm{PN^HP}$, and Fe(0) particles.[12] Bernskoetter and Hazari have also shown that $(^{i\mathrm{Pr}}\mathrm{PN^{Me}P})\mathrm{FeH_2(CO)}$ [$^{i\mathrm{Pr}}\mathrm{PN^{Me}P} = (i\mathrm{Pr_2PCH_2CH_2})_2\mathrm{NMe}$ (Chart 1)] is converted to an ∼1:1 mixture of $[(^{i\mathrm{Pr}}\mathrm{PN^{Me}P})\mathrm{FeH(CO)_2}][\mathrm{HCO_2}]$ and $^{i\mathrm{Pr}}\mathrm{PN^{Me}P}$ (along with an unknown precipitate) following catalytic dehydrogenation of formic acid and degassing the catalytic mixture.[8e]

We have recently reported the dehydrogenation of formic acid catalyzed by *cis*-$(^{i\mathrm{Pr}}\mathrm{PP^HP})\mathrm{FeH_2(CO)}$[8f] and *cis*-$(^{i\mathrm{Pr}}\mathrm{PP^{Me}P})\mathrm{FeH_2(CO)}$[8g] [$^{i\mathrm{Pr}}\mathrm{PP^HP} = (o\text{-}i\mathrm{Pr_2PC_6H_4})_2\mathrm{PH}$ and $^{i\mathrm{Pr}}\mathrm{PP^{Me}P} = (o\text{-}i\mathrm{Pr_2PC_6H_4})_2\mathrm{PMe}$, respectively (Chart 1)]. Without an acid, these PPP-ligated iron dihydride complexes can survive increased temperatures of 100−120 °C for days. However, in catalyzing formic acid dehydrogenation at 80 °C or even lower temperatures (e.g., 40 °C), they gradually lose catalytic activity. In this study, we have investigated the fate of the decomposed catalysts, including the identification of iron-containing species that were previously unaccounted for or thought to be catalytically inactive. These results can be informative for designing more effective iron-based, acid-tolerant catalysts in the future.

RESULTS AND DISCUSSION

Characterization of the Decomposed Catalysts. In the published work,[8f,g] we have shown that both *cis*-$(^{i\mathrm{Pr}}\mathrm{PP^HP})\mathrm{FeH_2(CO)}$ and *cis*-$(^{i\mathrm{Pr}}\mathrm{PP^{Me}P})\mathrm{FeH_2(CO)}$ undergo protonation with formic acid to release H_2. The resulting hydrido iron formate complexes can exist as multiple geometric isomers, all participating in hydrogen-bonding interactions with unreacted formic acid. The catalytic cycle (Scheme 1) is completed by a decarboxylation step to regenerate the iron dihydride species. According to our nuclear magnetic resonance (NMR) studies, the formate complexes are the resting state of the catalysts unless the concentration of formic acid is low or the catalytic reaction approaches completion. Regardless of the relative rates for the protonation and decarboxylation steps, the reaction solution should have a yellow to orange color, as expected for the formate and dihydride complexes. Consistent with this analysis, steady gas evolution was always accompanied by the observation of a colored reaction mixture in our catalytic studies.

Scheme 1. Proposed Catalytic Cycle for the PPP-Ligated Systems

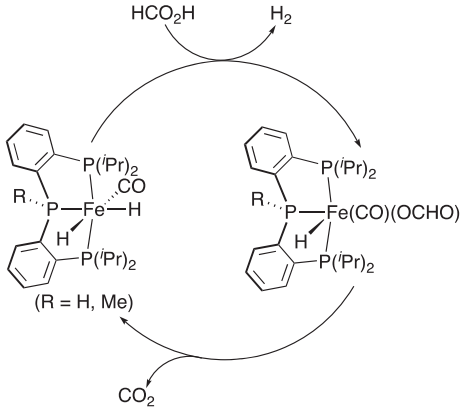

When the initial substrate:catalyst ratio was set at ≥1000 or successive addition of formic acid was implemented to maintain a low substrate:catalyst ratio (≤175), the reaction mixture (in 1,4-dioxane at 80 °C) eventually became cloudy and almost colorless. At that point, gas production slowed significantly. Both PPP-ligated systems exhibit this phenomenon. For this study, we decided to focus on the products degraded from *cis*-$(^{i\mathrm{Pr}}\mathrm{PP^{Me}P})\mathrm{FeH_2(CO)}$ and analyze the soluble component and the precipitate separately.

Soluble Component. The $^{31}\mathrm{P}\{^1\mathrm{H}\}$ NMR (in C_6D_6) spectrum is very complex (Figure S27), showing several resonances in the high-field region (5 to −35 ppm) associated with the unbound ligand and many resonances in the mid-field region (65 to 35 ppm) indicative of oxidized phosphorus centers. The main iron species with a fully bound $^{i\mathrm{Pr}}\mathrm{PP^{Me}P}$ ligand features a doublet at 108.1 ppm and a triplet at 95.7 ppm (J = 31.6 Hz) that integrate to ∼2:1. The most characteristic resonance in the ^{1}H NMR spectrum is a triplet of doublets at −11.50 ppm (J = 49.6 and 44.4 Hz), which supports an iron hydride coupled by the phosphorus nuclei of the $^{i\mathrm{Pr}}\mathrm{PP^{Me}P}$ ligand. Considering that $(^{i\mathrm{Pr}}\mathrm{PN^{Me}P})\mathrm{FeH_2(CO)}$ can decompose to form *cis*-$[(^{i\mathrm{Pr}}\mathrm{PN^{Me}P})\mathrm{FeH(CO)_2}][\mathrm{HCO_2}]$,[8e] we suspected that this hydride signal could be due to a similar compound bearing *cis*-$[(^{i\mathrm{Pr}}\mathrm{PP^{Me}P})\mathrm{FeH(CO)_2}]^+$. The presence of this cation was corroborated by the ESI-MS spectrum, in which the most intense ion has the expected mass-to-charge ratio (m/z) of 545.16 with fragment ions (MS^2) resulting from the loss of propene,[13] CO, and HCHO (or H_2 + CO). The hydrido iron dicarbonyl complex could be generated via a biomolecular process[14] involving a dinuclear intermediate.[12] It is, however, worth noting that dinuclear species or larger aggregates are absent from our decomposed catalyst, as confirmed by ESI-MS and diffusion-ordered NMR spectroscopy (DOSY).

To gain a better understanding of the roles that *cis*-$[(^{i\mathrm{Pr}}\mathrm{PP^{Me}P})\mathrm{FeH(CO)_2}]^+$ may play throughout the life of the catalyst, an independent synthesis of the cationic iron hydride was pursued (Scheme 2). The needed precursor, $(^{i\mathrm{Pr}}\mathrm{PP^{Me}P})\mathrm{Fe(CO)_2}$ (**1**), was readily prepared from $^{i\mathrm{Pr}}\mathrm{PP^{Me}P}$ and $\mathrm{Fe(CO)_5}$ following a synthetic procedure developed for $(^{i\mathrm{Pr}}\mathrm{PN^HP})\mathrm{Fe(CO)_2}$.[15] While the spectroscopic data are unsurprising, the crystal structure of **1** (Figure 1) reveals a unique coordination geometry around the iron center. On the basis of the geometry

https://doi.org/10.1021/acs.inorgchem.3c03125
Inorg. Chem. 2023, 62, 18714−18723

Scheme 2. Synthesis of the Cationic Iron Hydride with Different Counterions

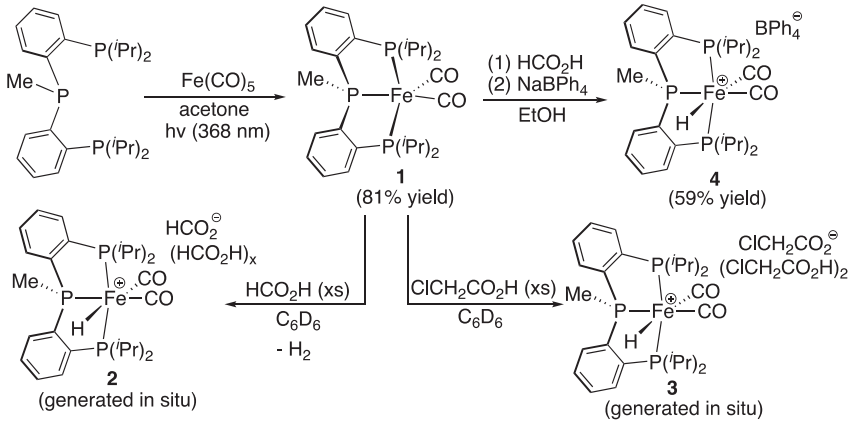

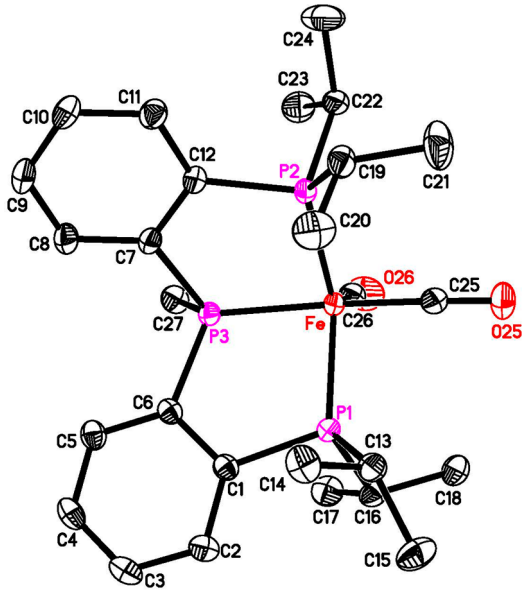

Figure 1. ORTEP of ($^{i\text{Pr}}$PP$^{\text{Me}}$P)Fe(CO)$_2$ (**1**) at the 50% probability level (hydrogen atoms have been omitted for clarity). Selected bond lengths (angstroms) and angles (degrees): Fe−C25, 1.7564(13); Fe−C26, 1.7561(13); Fe−P1, 2.1896(3); Fe−P2, 2.2051(3); Fe−P3, 2.1727(3); C25−O25, 1.1623(16); C26−O26, 1.1578(16); P1−Fe−P2, 133.081(13); P1−Fe−C26, 110.25(4); P2−Fe−C26, 116.14(4); P1−Fe−P3, 85.082(12); P2−Fe−P3, 85.042(12); P3−Fe−C25, 169.84(4); P3−Fe−C26, 94.13(4); C25−Fe−C26, 95.86(6); Fe−C25−O25, 177.59(12); Fe−C26−O26, 176.73(12).

index[16] (τ_5 = 0.61), iron is situated in a distorted trigonal bipyramidal (TBP) coordination sphere with the two axial positions occupied by the central phosphorus and a CO ligand [P−Fe−CO angle of 169.84(4)°]. In contrast, ($^{i\text{Pr}}$PN$^{\text{H}}$P)Fe(CO)$_2$ adopts a distorted square pyramidal (SQP) structure with one of the CO ligands occupying the apical site.[15] The closely related ($^{i\text{Pr}}$PN$^{\text{Me}}$P)Fe(CO)$_2$[17] and the pyridine-based complexes, ($^{i\text{Pr}}$PN$_{\text{pyr}}$P)Fe(CO)$_2$ [$^{i\text{Pr}}$PN$_{\text{pyr}}$P = 2,6-(^{i}Pr$_2$PCH$_2$)$_2$(C$_5$H$_3$N)][18] and ($^{i\text{Pr}}$P$^{\text{N}}$N$_{\text{pyr}}{}^{\text{N}}$P)Fe(CO)$_2$ [$^{i\text{Pr}}$P$^{\text{N}}$N$_{\text{pyr}}{}^{\text{N}}$P = 2,6-(^{i}Pr$_2$PNR)$_2$(C$_5H_3$N) (R = H or Me)],[19] also have a TBP molecular geometry; however, the axial sites are defined by the two phosphorus donors. The unusual geometry observed with **1** likely reflects a more folded ligand structure caused by the central phosphorus. In fact, the P1−Fe−P2 angle of 133.081(13)° in **1** is the smallest among all of the iron dicarbonyl complexes mentioned above.

The conversion of **1** into *cis*-[($^{i\text{Pr}}$PP$^{\text{Me}}$P)FeH(CO)$_2$]$^+$ was first studied by treating the iron dicarbonyl complex with excess formic acid (Scheme 2), which resulted in a rapid color change from orange to almost colorless. Attempts to isolate cationic iron hydride in the solid form were fruitless. Removing the solvent under vacuum restored **1** along with some decomposition products, indicating that protonation of the iron center is a reversible process. A mixture of **1** and formic acid (large excess) kept in toluene and pentane led to the formation of crystals, which were analyzed by X-ray diffraction as the previously known Fe(OCHO)$_2$·$^1/_3$HCO$_2$H.[20] Despite the challenges, *cis*-[($^{i\text{Pr}}$PP$^{\text{Me}}$P)FeH(CO)$_2$]$^+$ can be readily generated in solution by mixing **1** with formic acid in C$_6$D$_6$ and characterized by NMR spectroscopy (or generated in methanol and analyzed by ESI-MS). The hydride and phosphorus resonances match those described earlier for the main iron species present in the decomposed catalyst. Interestingly, H$_2$ (4.47 ppm) was also detected from the reaction mixture, which may be explained by a second protonation step involving the newly formed hydride ligand in *cis*-[($^{i\text{Pr}}$PP$^{\text{Me}}$P)FeH(CO)$_2$]$^+$. Alternatively, H$_2$ could be produced from the dehydrogenation of formic acid, presumably catalyzed by *cis*-[($^{i\text{Pr}}$PP$^{\text{Me}}$P)FeH(CO)$_2$]$^+$. We ruled out the first scenario on the basis of the observation that chloroacetic acid (pK_a = 2.87), which is more acidic than formic acid (pK_a = 3.75) but unlikely to undergo dehydrogenation, reacted with **1** to give *cis*-[($^{i\text{Pr}}$PP$^{\text{Me}}$P)FeH(CO)$_2$]$^+$ without forming H$_2$.

The cationic iron hydride generated from **1** and chloroacetic acid in toluene was layered with pentane and then kept at −30 °C, which produced crystals suitable for X-ray crystallographic study. This allowed us not only to further confirm the *anti* Me−P−Fe−H configuration as suggested by nuclear Overhauser effect spectroscopy (NOESY) but also to understand the nature of the counterion. As shown in Figure 2, the chloroacetate anion is hydrogen-bonded to two chloroacetic acid molecules. This type of hydrogen-bonding interactions was previously observed with ($^{i\text{Pr}}$PP$^{\text{Me}}$P)FeH(CO)(OCHO),[8g] although in that case the formate ion is coordinated to iron. Given these results, we propose that the protonation of **1** with formic acid gives rise to *cis*-[($^{i\text{Pr}}$PP$^{\text{Me}}$P)FeH(CO)$_2$][(HCO$_2$)(HCO$_2$H)$_x$] (**2**), where the formate ion also forms hydrogen bonds with the unreacted formic acid. The hydrogen-bonding network, [(HCO$_2$)-(HCO$_2$H)$_x$]$^-$, may have additional interactions with the cation,

https://doi.org/10.1021/acs.inorgchem.3c03125
Inorg. Chem. 2023, 62, 18714−18723

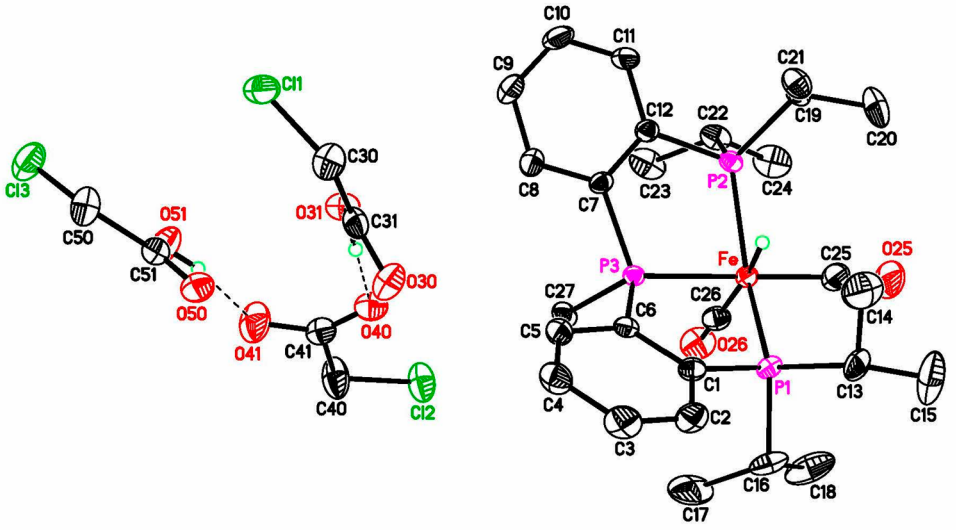

Figure 2. ORTEP of *cis*-[($^{i\text{Pr}}$PP$^{\text{Me}}$P)FeH(CO)$_2$][(ClCH$_2$CO$_2$)(ClCH$_2$CO$_2$H)$_2$] (**3**) at the 50% probability level (for clarity, all hydrogen atoms have been omitted, except the hydride and those involved in the hydrogen-bonding interactions). Selected bond lengths (angstroms) and angles (degrees): Fe−H, 1.419(38); Fe−C25, 1.782(3); Fe−C26, 1.793(3); Fe−P1, 2.2255(7); Fe−P2, 2.2225(6); Fe−P3, 2.2076(6); C25−O25, 1.142(3); C26−O26, 1.135(3); P1−Fe−P2, 147.96(3); P1−Fe−P3, 86.00(2); P2−Fe−P3, 86.03(2); P3−Fe−C25, 179.58(10); P3−Fe−C26, 90.25(9); C25−Fe−C26, 90.17(13); Fe−C25−O25, 175.1(3); Fe−C26−O26, 179.6(3).

which can be used to rationalize the difficulty in obtaining a good-quality ^{13}C{^{1}H} NMR spectrum for **2** (Figure S7). The dehydrogenation of formic acid occurring in the background changes the HCO_2^-:HCO_2H ratio continuously and fast enough to shift the carbon resonances between the scans.

To avoid the complication of $[(HCO_2)(HCO_2H)_x]^-$, in situ-generated complex **2** was subjected to an anion exchange reaction with $NaBPh_4$ (Scheme 2) to afford *cis*-[($^{i\text{Pr}}$PP$^{\text{Me}}$P)-FeH(CO)$_2$]BPh_4 (**4**). The product can now be isolated in solid form and characterized by ^{13}C{^{1}H} NMR spectroscopy, in addition to other spectroscopic methods and elemental analysis (see Experimental Section for details). As expected, the structure of *cis*-[($^{i\text{Pr}}$PP$^{\text{Me}}$P)FeH(CO)$_2$]$^+$ in **4** (Figure 3) is very similar to that in **3**. Minor differences may arise from weak interactions between the phenyl groups in BPh_4 and the methyl groups in $^{i\text{Pr}}$PP$^{\text{Me}}$P, which increase the P3−Fe−C26, C25−Fe−C26, and P1−Fe−P2 angles by 2.6°, 2.1°, and 4.0°, respectively.

The decomposition of **2** to Fe(OCHO)$_2$·$^1/_3$$HCO_2H$ should release $^{i\text{Pr}}$PP$^{\text{Me}}$P, which in the presence of formic acid or during the catalytic reaction is unlikely to exist in the free ligand form. The pK_a values for the conjugate acids of the model phosphines, $MePPh_2$ (pK_a = 4.59) and Me_2PPh (pK_a = 6.49),[21] suggest that all three phosphorus centers, especially the peripheral ones (i.e., in P^{i}Pr$_2$), can potentially be protonated by formic acid (pK_a = 3.75). As illustrated in Figure 4, the ^{31}P{^{1}H} NMR spectrum of $^{i\text{Pr}}$PP$^{\text{Me}}$P in C_6D_6 features an AB_2 spin system with minor second-order effects. The addition of formic acid (∼8 equiv) shifts the resonance of the periphery phosphorus slightly (P^{i}Pr$_2$, −2.2 ppm → −1.1 ppm; PMe, −35.9 → −36.2 ppm; $\Delta\nu/J$, 39 → 41) but enough to change the splitting pattern to one more typical of an AX_2 spin system. This result is also consistent with the ESI-MS data acquired for the decomposed catalyst, showing an ion with an m/z value of 479.24 that can be attributed to protonated ligand [$^{i\text{Pr}}$PP$^{\text{Me}}$P + HCO_2H + H]$^+$.

The ESI-MS spectrum of the decomposed catalyst also displays ions for the monooxidized ligand (m/z 449.23) and

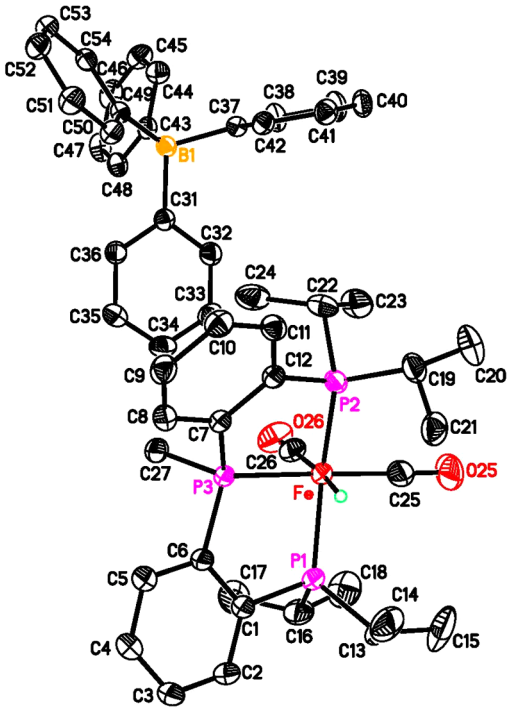

Figure 3. ORTEP of *cis*-[($^{i\text{Pr}}$PP$^{\text{Me}}$P)FeH(CO)$_2$]BPh_4 (**4**) at the 50% probability level (all hydrogen atoms except that bound to iron have been omitted for clarity; only the major component is shown for the disordered C23 atom). Selected bond lengths (angstroms) and angles (degrees): Fe−H, 1.468(20); Fe−C25, 1.7742(17); Fe−C26, 1.7902(17); Fe−P1, 2.2287(4); Fe−P2, 2.2309(4); Fe−P3, 2.2186(4); C25−O25, 1.146(2); C26−O26, 1.145(2); P1−Fe−P2, 151.996(19); P1−Fe−P3, 85.791(15); P2−Fe−P3, 85.540(15); P3−Fe−C25, 174.83(6); P3−Fe−C26, 92.86(5); C25−Fe−C26, 92.30(8); Fe−C25−O25, 177.19(19); Fe−C26−O26, 178.05(15).

https://doi.org/10.1021/acs.inorgchem.3c03125
Inorg. Chem. 2023, 62, 18714−18723

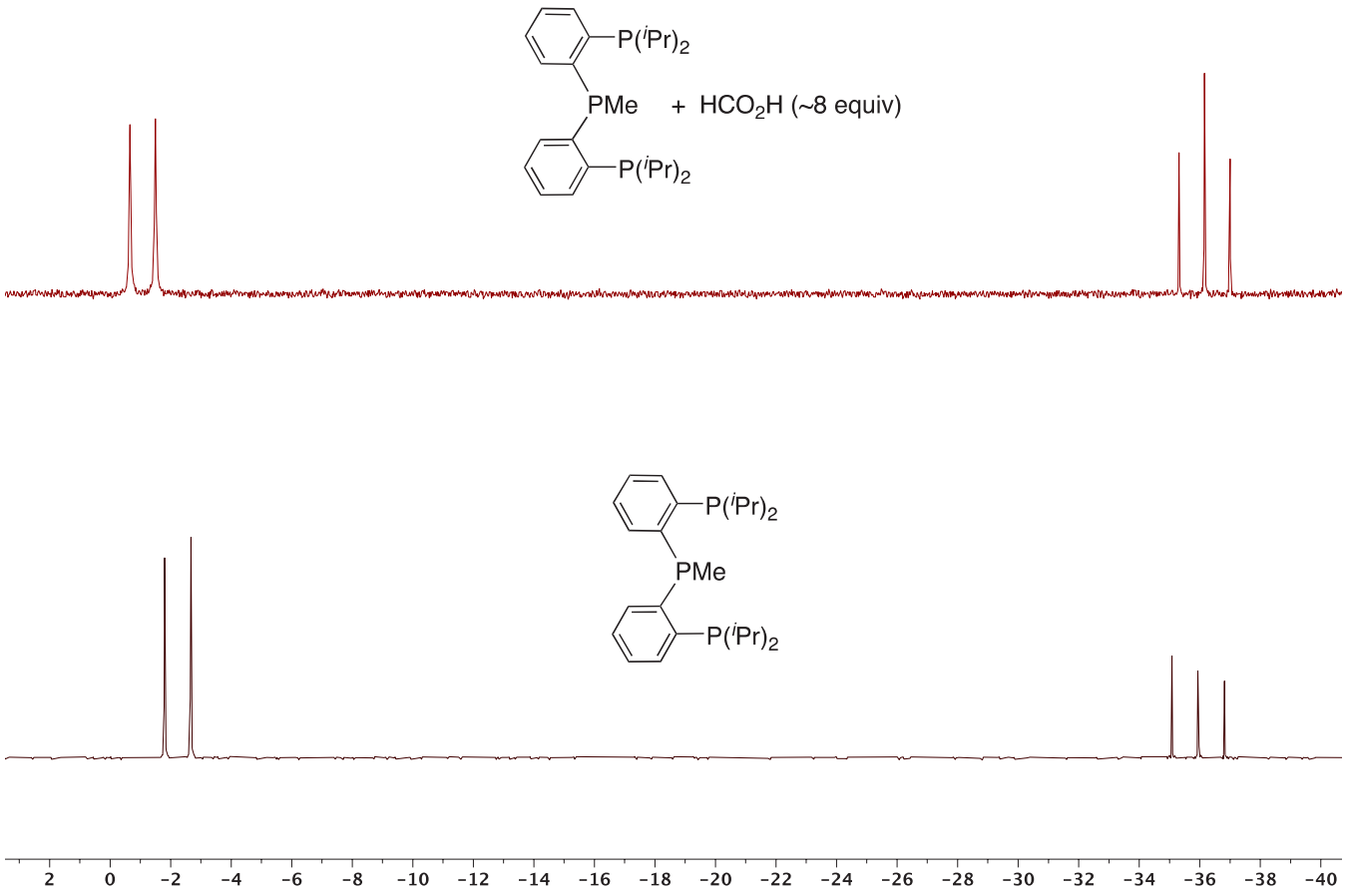

Figure 4. $^{31}P\{^{1}H\}$ NMR spectra of $^{i\text{Pr}}PP^{\text{Me}}P$ in C_6D_6 (spectrum at the bottom, the free ligand; spectrum at the top, after formic acid was added).

monooxidized *cis*-$[(^{i\text{Pr}}PP^{\text{Me}}P)FeH(CO)_2]^+$ (m/z 561.15). Control experiments confirm that $^{i\text{Pr}}PP^{\text{Me}}P$ is inert to CO_2 and H_2 (1 bar, at 80 °C), the two gaseous molecules produced during the formic acid hydrogenation reaction. To our surprise, at room temperature, the C_6D_6 solution of $^{i\text{Pr}}PP^{\text{Me}}P$ tolerated air (for ≥18 h) that was intentionally introduced into the NMR tube. However, heating the solution to 80 °C for 18 h led to low-intensity phosphorus resonances appearing at 29.8 ppm (triplet, J = 11 Hz) and −1.5 ppm (doublet, J = 11 Hz), implying that oxidation takes place at the central phosphorus site (∼10% oxidation) but at a rate significantly slower than the rate of catalyst degradation. Oxidation of the catalyst during ESI-MS sampling and analysis is unlikely to happen because **2** generated in situ and analyzed under the same conditions gave no oxidized ions (Figure S10). Taken together, we propose the following. (1) The iron catalyst can be degraded by the adventitious O_2 present in the reaction vessel, and (2) the oxidation process occurs under the catalytic conditions and when the ligand remains (fully or partially) bound to iron. The combination of oxidation, dissociation, and protonation events at the phosphorus centers must contribute to the complexity of the phosphorus resonances observed in the high-field and mid-field regions.

Precipitate. Given that **2** (in toluene and pentane, with excess formic acid) decomposes to yield $Fe(OCHO)_2{\cdot}^1/_3HCO_2H$, we suspected that the precipitate obtained from the decomposed catalyst could be some form of iron formate. Following a literature procedure,[22] $Fe(OCHO)_2{\cdot}2H_2O$ was prepared under an inert atmosphere from iron powder and formic acid (aqueous). However, it shows infrared (IR) bands that are inconsistent with those of the precipitate. Because the catalytic reaction is typically performed in 1,4-dioxane with a low moisture level, it is possible that the iron formate is solvated by 1,4-dioxane ($C_4H_8O_2$). Heating $Fe(OCHO)_2{\cdot}2H_2O$ in 1,4-dioxane at 80 °C in the presence of formic acid (needed to prevent decomposition) allowed the isolation of $Fe(OCHO)_2{\cdot}^1/_4C_4H_8O_2$, which indeed gives IR bands identical to those for the precipitate (Figure S33). The remaining IR bands displayed by the precipitate can be identified as vibrational modes for the residual formic acid. It should be noted that $Fe(OCHO)_2{\cdot}^1/_3HCO_2H$ and $Fe(OCHO)_2{\cdot}2H_2O$ adopt completely different structures (Chart 2). The former involves four unique iron centers with each formate ligand bridging three Fe atoms and the formic acid filling the void space.[20] In contrast, $Fe(OCHO)_2{\cdot}2H_2O$ bears two unique iron centers. One Fe atom is coordinated by six formate ligands that bridge to the second Fe center. In addition to the two bridging formate ligands, this second Fe is coordinated by four water molecules.[23] Although we have yet to obtain the crystal structure of $Fe(OCHO)_2{\cdot}^1/_4C_4H_8O_2$, the IR spectrum suggests that its structure resembles that of $Fe(OCHO)_2{\cdot}^1/_3HCO_2H$ with 1,4-dioxane simply being trapped in the lattice. This explains why $Fe(OCHO)_2{\cdot}2H_2O$ and $Fe(OCHO)_2{\cdot}^1/_4C_4H_8O_2$ feature different IR bands associated with the formate ligands (e.g., ν_{OCO}, δ_{CH}, and δ_{OCO} bands).

https://doi.org/10.1021/acs.inorgchem.3c03125
Inorg. Chem. 2023, 62, 18714−18723

Chart 2. Structures of $Fe(OCHO)_2 \cdot {}^1/_3HCO_2H$ (left) and $Fe(OCHO)_2 \cdot 2H_2O$ (right) Illustrating Different Coordination Modes Adopted by the Formate

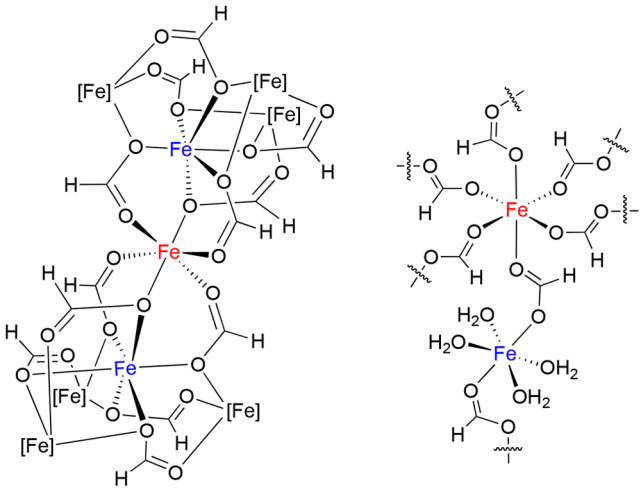

Neary and Parkin have shown that, under heating, $Ni(OCHO)_2 \cdot 2H_2O$ can react with PMe_3 to give $Ni(PMe_3)_4$, which in turn catalyzes the dehydrogenation of formic acid.[24] Our attempts to use the same strategy to synthesize PPP-ligated iron complexes from $Fe(OCHO)_2 \cdot 2H_2O$, $^{i\mathrm{Pr}}PP^{\mathrm{Me}}P$, and CO (1 bar) were unsuccessful. We attribute the failure to the poor solubility of $Fe(OCHO)_2 \cdot 2H_2O$ in 1,4-dioxane (<1 mg/100 mL) or THF. The mechanistic implication is that, once $Fe(OCHO)_2 \cdot {}^1/_4C_4H_8O_2$ precipitates from the catalytic mixture, it is unlikely converted back to PPP-ligated iron complexes to participate in the catalytic reaction again.

Catalytic Activity. Having identified that *cis*-($^{i\mathrm{Pr}}PP^{\mathrm{Me}}P$)$FeH_2(CO)$ decomposes with formic acid to form **2** and $Fe(OCHO)_2 \cdot {}^1/_4C_4H_8O_2$, we shifted our attention to their catalytic activity. Iron dicarbonyl complex **1** and $Fe(OCHO)_2 \cdot 2H_2O$ were used as surrogates because, under the catalytic conditions, they would be rapidly converted into **2** and $Fe(OCHO)_2 \cdot {}^1/_4C_4H_8O_2$, respectively. As summarized in Table 1, **1** remains active for catalytic dehydrogenation of formic acid, giving a TON of 8 in 1 h and a TON of 24 in 18 h (entry 3). Granted, it is far more inefficient as a catalyst than *cis*-($^{i\mathrm{Pr}}PP^{\mathrm{Me}}P$)$FeH_2(CO)$ (entry 1). Cationic iron hydride **4** is as active as **1** (entry 4), whereas the iron formate is completely inactive (entry 5). In our previous studies, we have shown that *cis*-($^{i\mathrm{Pr}}PP^{\mathrm{H}}P$)$FeH_2(CO)$ outperforms *cis*-($^{i\mathrm{Pr}}PP^{\mathrm{Me}}P$)$FeH_2(CO)$ (entry 2 vs entry 1) due to slightly higher stability in formic acid.[8f,g] The same trend holds when comparing ($^{i\mathrm{Pr}}PP^{\mathrm{H}}P$)$Fe(CO)_2$ [**5**, prepared from $^{i\mathrm{Pr}}PP^{\mathrm{H}}P$ and $Fe(CO)_5$] with **1** (entry 6 vs entry 3). The PPP-type ligands are needed for iron to promote the dehydrogenation reaction; a control experiment with $Fe(CO)_5$ confirms that the simple iron carbonyl is unable to catalyze the release of H_2 from formic acid (entry 7). Without iron, the ligand itself cannot be a catalyst (entry 8).

Mechanistic Consideration. The catalytic activity observed with **1**, **4**, and **5**, albeit limited, is very intriguing, because on the basis of previous mechanistic understanding[8e,12,14,17] catalysts would be pronounced dead once reaching the iron dicarbonyl or hydrido iron dicarbonyl stage. As mentioned above, the room-temperature reaction of **1** with excess formic acid produces H_2 while forming **2**. To further confirm that CO_2 is the other product from the formic acid dehydrogenation and the dehydrogenation reaction is catalyzed by *cis*-[($^{i\mathrm{Pr}}PP^{\mathrm{Me}}P$)$FeH(CO)_2]^+$, **4** was treated with 15 equiv of $H^{13}CO_2H$. For solubility reasons, a mixed solvent of C_6D_6 and CD_2Cl_2 (1:4.5) was employed. Even at room temperature, both $^{13}CO_2$ (δ_C 124.97) and H_2 (δ_H 4.48) were observed in the NMR spectra.

Table 1. Dehydrogenation of Formic Acid Catalyzed by Different Iron Species[a]

$$HCO_2H \xrightarrow[1,4\text{-dioxane, } 80\ ^\circ C]{0.1\ \text{mol\% [Fe]}} H_2 + CO_2$$

entry	[Fe]	TOF_{1h} (conversion)[d,e]	TON_{max} (time, conversion)[e,f]
1[b]	*cis*-($^{i\mathrm{Pr}}PP^{\mathrm{Me}}P$)$Fe(CO)H_2$	439 (44%)	768 (8 h, 77%)
2[c]	*cis*-($^{i\mathrm{Pr}}PP^{\mathrm{H}}P$)$Fe(CO)H_2$	473 (47%)	859 (8 h, 86%)
3	($^{i\mathrm{Pr}}PP^{\mathrm{Me}}P$)$Fe(CO)_2$ (**1**)	8 (1%)	24 (18 h, 2%)
4	*cis*-[($^{i\mathrm{Pr}}PP^{\mathrm{Me}}P$)$FeH(CO)_2]BPh_4$ (**4**)	8 (1%)	24 (18 h, 2%)
5	$Fe(OCHO)_2 \cdot 2H_2O$	0 (0%)	N/A
6	($^{i\mathrm{Pr}}PP^{\mathrm{H}}P$)$Fe(CO)_2$ (**5**)	15 (2%)	108 (18 h, 11%)
7	$Fe(CO)_5$	0 (0%)	N/A
8	$^{i\mathrm{Pr}}PP^{\mathrm{Me}}P$	0 (0%)	N/A

[a]Standard conditions: HCO_2H (100 μL, 98−100% purity, 2.65 mmol) and an iron catalyst (0.1 mol %) mixed in 1,4-dioxane (0.5 mL). [b]Reported in ref 8g. [c]Reported in ref 8f. [d]TOF_{1h} is the calculated turnover frequency after 1 h. [e]Average of two runs. [f]TON_{max} is the turnover number obtained when gas production ceases.

Two distinct mechanistic pathways that can explain the catalytic role of *cis*-[($^{i\mathrm{Pr}}PP^{\mathrm{Me}}P$)$FeH(CO)_2]^+$ are outlined in Scheme 3 (for clarity, hydrogen-bonding interactions are not shown). In cycle A, the hydride ligand in *cis*-[($^{i\mathrm{Pr}}PP^{\mathrm{Me}}P$)$FeH(CO)_2]^+$ participates in a protonation reaction with formic acid to give H_2 and [($^{i\mathrm{Pr}}PP^{\mathrm{Me}}P$)$Fe(CO)_2(OCHO)]^+$, which subsequently undergoes decarboxylation to regenerate the catalyst. Alternatively, dissociation of CO from *cis*-[($^{i\mathrm{Pr}}PP^{\mathrm{Me}}P$)$FeH(CO)_2]^+$ creates a vacant coordination site that can be occupied by the formate ion, allowing the iron complex to re-enter the catalytic cycle proposed for *cis*-($^{i\mathrm{Pr}}PP^{\mathrm{Me}}P$)$FeH_2(CO)$ (cycle B). The lack of reactivity of **2** and **4** toward $ClCH_2CO_2H$ (room temperature or 80 °C) suggests that protonating the hydride ligand in *cis*-[($^{i\mathrm{Pr}}PP^{\mathrm{Me}}P$)$FeH(CO)_2]^+$ is difficult, and cycle A is unlikely to operate here.

Next, the possibility for dissociation of CO from *cis*-[($^{i\mathrm{Pr}}PP^{\mathrm{Me}}P$)$FeH(CO)_2]^+$ was probed by exposing **2** (in C_6D_6) and **4** (in CD_2Cl_2) to ^{13}CO (1 bar) at 80 °C. Interestingly, ^{13}CO incorporation was observed with only **2**. Under the same conditions, five-coordinate complex **1** failed to undergo ligand exchange with ^{13}CO, suggesting that deprotonation of **2** by the counterion to form **1** is not the reason for ^{13}CO being incorporated into **2**. At this point, we do not fully understand the effect of the counterion on the rate of $^{12}CO/^{13}CO$ scrambling. Nevertheless, the ability of **2** to exchange ^{12}CO with ^{13}CO supports the viability of re-entering cycle B by the cationic iron hydride species. Under the catalytic conditions where formic acid is used in large excess, **4** can readily exchange its anion for $[(HCO_2)(HCO_2H)_x]^-$ to initiate CO dissociation. The

https://doi.org/10.1021/acs.inorgchem.3c03125
Inorg. Chem. 2023, 62, 18714−18723

Scheme 3. Two Plausible Catalytic Cycles for the Dehydrogenation Reaction

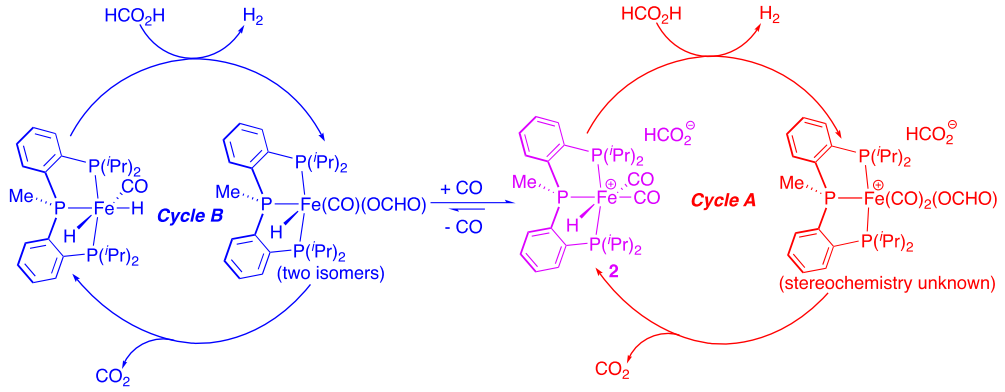

Scheme 4. Formation of 2 from Protonation of 1 or Anion Exchange with 4

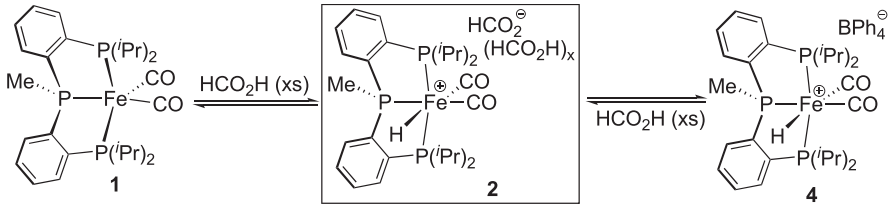

convergence of **1** and **4** to **2** (Scheme 4) is also consistent with the fact that **1** and **4** show very similar catalytic activity.

During the catalytic reaction, how does a species such as **2** form in the first place? A close inspection of the reaction between *cis*-($^{i\text{Pr}}$PP$^{\text{Me}}$P)FeH$_2$(CO) and formic acid (5.5 equiv) in 1,4-dioxane (with several drops of C_6D_6 added to lock the NMR signal) confirms that protonated $^{i\text{Pr}}$PP$^{\text{Me}}$P emerges from the reaction mixture before **2** can be detected. Without the supporting ligand, $^{i\text{Pr}}$PP$^{\text{Me}}$P, iron-containing intermediates are presumably converted into iron formate while releasing CO, as demonstrated by a model compound, Fe(CO)$_5$. The released CO can potentially react with *cis*-($^{i\text{Pr}}$PP$^{\text{Me}}$P)FeH$_2$(CO) and ($^{i\text{Pr}}$PP$^{\text{Me}}$P)FeH(CO)(OCHO) to produce ($^{i\text{Pr}}$PP$^{\text{Me}}$P)Fe(CO)$_2$ and [($^{i\text{Pr}}$PP$^{\text{Me}}$P)FeH(CO)$_2$][HCO$_2$], respectively, which become **2** when formic acid is present. Indeed, exposing *cis*-($^{i\text{Pr}}$PP$^{\text{Me}}$P)FeH$_2$(CO) in C_6D_6 to CO (1 bar) at 80 °C leads to the formation of ($^{i\text{Pr}}$PP$^{\text{Me}}$P)Fe(CO)$_2$ (15% conversion in 16 h). A similar experiment with the in situ-generated ($^{i\text{Pr}}$PP$^{\text{Me}}$P)FeH(CO)(OCHO) (contains formic acid) produces both ($^{i\text{Pr}}$PP$^{\text{Me}}$P)Fe(CO)$_2$ and **2**.

CONCLUSIONS

In summary, we have conducted an in-depth study of how PPP-ligated iron catalysts degrade during the dehydrogenation of formic acid. Although we have focused specifically on the $^{i\text{Pr}}$PP$^{\text{Me}}$P ligand platform, the identification of Fe(OCHO)$_2$ at the final stage of the catalysts is broadly implicated in other iron-based catalytic systems. What we have found to be surprising is that *cis*-[($^{i\text{Pr}}$PP$^{\text{Me}}$P)FeH(CO)$_2$]$^+$, a species formed during the degradation process, remains catalytically active. The formation of Fe(OCHO)$_2$ and *cis*-[($^{i\text{Pr}}$PP$^{\text{Me}}$P)FeH(CO)$_2$]$^+$ is triggered by the dissociation of the PPP-type supporting ligand and exacerbated by the release of CO. Our future efforts will be devoted to building iron-based catalysts with stronger binding by the supporting ligands.

EXPERIMENTAL SECTION

General Methods. Unless otherwise noted, all organometallic compounds were prepared and handled under an argon atmosphere by using standard glovebox and Schlenk techniques. Dry and oxygen-free pentane and toluene were collected from an Innovative Technology solvent purification system and used throughout the experiments. Acetone, ethanol, and 1,4-dioxane were dried over 4 Å molecular sieves and deoxygenated by bubbling argon through them for 1 h prior to use. Formic acid (98−100%) was purchased from Sigma-Aldrich and deoxygenated via freeze−pump−thaw cycles. Benzene-d_6 (99.5% D) was dried over sodium benzophenone and distilled under an argon atmosphere. Dichloromethane-d_2 (99.8% D) was purchased from Cambridge Isotope Laboratories, Inc. Carbon monoxide-^{13}C (≥99% ^{13}C) and formic acid-^{13}C (95% purity, 99% ^{13}C) were purchased from Sigma-Aldrich. These isotopically labeled reagents were used as received without further purification. $^{i\text{Pr}}$PP$^{\text{Me}}$P,[25] $^{i\text{Pr}}$PP$^{\text{H}}$P,[26] and Fe(OCHO)$_2$·2H$_2$O[22] were prepared as described in the literature. NMR spectra were recorded on a Bruker AV400 or Bruker NEO400 NMR spectrometer. The chemical shift values for the ^{1}H and ^{13}C{^{1}H} NMR spectra were referenced internally to the residual solvent resonances. ^{31}P{^{1}H} NMR spectra were referenced externally to 85% H_3PO_4 (0 ppm). IR spectra were recorded on a PerkinElmer Spectrum Two Fourier transform infrared spectrometer equipped with a Smart Orbit diamond attenuated-total-reflectance (ATR) accessory. Electrospray ionization mass spectra (ESI-MS) were recorded on a Thermo Scientific LTQ-FT hybrid mass spectrometer that combines a linear ion trap and Fourier transform ion cyclotron resonance technologies.

Decomposition of the Catalyst. In a glovebox, to an oven-dried 10 mL Schlenk tube were added *cis*-($^{i\text{Pr}}$PP$^{\text{Me}}$P)FeH$_2$(CO) (10 mg) and 1,4-dioxane (2 mL). The tube was removed from the glovebox and attached to a gas buret filled with mineral oil. Formic acid (400 μL) was added via a microliter syringe, after which the tube was immersed in an oil bath preheated to 80 °C. When formic acid was fully consumed, another portion of the acid (400 μL) was added. This process was repeated until gas production slowed significantly, and the reaction mixture became cloudy and light in color. The soluble component and

https://doi.org/10.1021/acs.inorgchem.3c03125
Inorg. Chem. 2023, 62, 18714−18723

precipitate were separated and analyzed by NMR and IR spectrscopy, respectively. In a separate experiment, the cloudy mixture was evaporated to dryness under vacuum, and the resulting off-white, sticky substance was analyzed by ESI-MS.

Synthesis of ($^{i\mathrm{Pr}}$PP$^{\mathrm{Me}}$P)Fe(CO)$_2$ (1). In a glovebox, to an oven-dried 50 mL Schlenk flask were added $^{i\mathrm{Pr}}$PP$^{\mathrm{Me}}$P (50 mg, 0.12 mmol), Fe(CO)$_5$ (16 μL, 0.12 mmol), and acetone (5 mL). The flask was removed from the glovebox, connected to a Schlenk line, and subjected to ultraviolet (UV) radiation by using an array of four 368 nm UV LEDs (caution: UV light safety glasses should be worn). After UV irradiation for 1 h, the volatiles were removed under vacuum. Washing the residue with cold pentane (0 °C, 3 × 5 mL) followed by drying under vacuum yielded the desired product as a bright orange powder (51 mg, 81% yield). X-ray-quality crystals were grown from a toluene/pentane solution kept at −30 °C. ^{1}H NMR (400 MHz, C_6D_6): δ 7.69 (t, J = 6.4 Hz, Ar*H*, 2H), 7.32−7.27 (m, Ar*H*, 2H), 7.13−7.00 (m, Ar*H*, 4H), 2.54−2.44 [m, C*H*(CH$_3$)$_2$, 2H], 2.41−2.30 [m, C*H*(CH$_3$)$_2$, 2H], 1.78 (d, $^2J_{H-P}$ = 8.0 Hz, PC*H*$_3$, 3H), 1.52−1.45 [m, CH(C*H*$_3$)$_2$, 6H], 1.22−1.15 [m, CH(C*H*$_3$)$_2$, 6H], 0.85−0.78 [m, CH(C*H*$_3$)$_2$, 12H]. ^{13}C{^{1}H} NMR (101 MHz, C_6D_6): δ 233.1 (td, $^2J_{C-P}$ = 28.1 and 26.4 Hz, *C*O), 222.8 (dt, $^2J_{C-P}$ = 22.9 and 10.6 Hz, *C*O), 148.7 (ddd, J = 40.4, 25.1, and 24.2 Hz, Ar*C* bonded to P), 147.8 (ddd, J = 47.7, 16.2, and 13.8 Hz, Ar*C* bonded to P), 129.6 (d, J = 4.6 Hz, Ar*C*), 129.2−129.1 (m, Ar*C*), 128.7−127.8 (m, Ar*C*), 33.1 [t, J = 13.2 Hz, *C*H(CH$_3$)$_2$], 31.6 [t, J = 8.4 Hz, CH(*C*H$_3$)$_2$], 22.6 (d, $^1J_{C-P}$ = 30.1 Hz, P*C*H$_3$), 20.2 [t, J = 2.8 Hz, CH(*C*H$_3$)$_2$], 19.9 [s, CH(*C*H$_3$)$_2$], 19.6 [t, J = 3.2 Hz, CH(*C*H$_3$)$_2$], 18.7 [s, CH(*C*H$_3$)$_2$]. ^{31}P{^{1}H} NMR (162 MHz, C_6D_6): δ 117.0 (AB_2 spin, J_{AB} = 63.2 Hz, P^{i}Pr$_2$, 2P), 110.5 (AB_2 spin, J_{AB} = 63.2 Hz, *P*Me, 1P). Selected ATR-IR data (solid, cm^{-1}): 1889 ($\nu_{C\equiv O}$), 1836 ($\nu_{C\equiv O}$). Anal. Calcd for $C_{27}H_{39}O_2P_3Fe$: C, 59.57; H, 7.22. Found: C, 59.28; H, 7.24.

***cis*-[($^{i\mathrm{Pr}}$PP$^{\mathrm{Me}}$P)FeH(CO)$_2$][(HCO$_2$)(HCO$_2$H)$_x$] (2) Generated In Situ.** In a glovebox, to a screw-cap NMR tube were added **1** (5.4 mg, 0.010 mmol) and ∼0.5 mL of C_6D_6, which formed an orange solution. The NMR tube was sealed with a PTFE septum and removed from the glovebox. Formic acid (10 μL, 0.27 mmol) was injected through the septum via a microliter syringe, resulting in a rapid color change from orange to almost colorless. Efforts to isolate the product in a solid form were thwarted by the reversible nature of the reaction as well as decomposition. As a result, the protonation product was characterized only in solution by NMR and ESI-MS. ^{1}H NMR (400 MHz, C_6D_6): δ 11.02 (s, excess HCO$_2$*H*), 8.44 (t, J = 8.0 Hz, Ar*H*, 2H), 7.71 (t, J = 7.6 Hz, Ar*H*, 2H), 7.44 (s, excess *H*CO$_2$H), 7.39 (t, J = 8.0 Hz, Ar*H*, 2H), 7.25−7.21 (m, Ar*H*, 2H), 2.36−2.25 [m, C*H*(CH$_3$)$_2$, 2H], 2.18−2.05 [m, C*H*(CH$_3$)$_2$, 2H], 1.69 (d, $^2J_{H-P}$ = 8.8 Hz, PC*H*$_3$, 3H), 1.02−0.94 [m, CH(C*H*$_3$)$_2$, 6H], 0.92−0.84 [m, CH(C*H*$_3$)$_2$, 6H], 0.73−0.65 [m, CH(C*H*$_3$)$_2$, 6H], 0.57−0.48 [m, CH(C*H*$_3$)$_2$, 6H], −11.50 (td, $^2J_{H-P}$ = 49.2 and 44.4 Hz, Fe*H*, 1H); H$_2$ (δ 4.47) was also detected from the sample. ^{13}C{^{1}H} NMR (101 MHz, C_6D_6): δ 213.5−211.5 (m, *C*O), 166.3−164.0 (m, O*C*HO), 143.5−139.9 (m, Ar*C* bonded to P), 133.6−129.7 (m, Ar*C*), 31.5−30.0 [m, *C*H(CH$_3$)$_2$], 21.8 (d, $^1J_{C-P}$ = 32.3 Hz, PCH$_3$), 19.1 [s, CH(*C*H$_3$)$_2$], 18.4 [s, CH(*C*H$_3$)$_2$], 18.3 [s, CH(*C*H$_3$)$_2$], 18.1 [s, CH(*C*H$_3$)$_2$]. ^{31}P{^{1}H} NMR (162 MHz, C_6D_6): δ 107.9 (d, $^2J_{P-P}$ = 31.8 Hz, P^{i}Pr$_2$, 2P), 95.6 (t, $^2J_{P-P}$ = 31.8 Hz, *P*Me, 1P). ESI-MS of **2** generated in MeOH (m/z): [($^{i\mathrm{Pr}}$PP$^{\mathrm{Me}}$P)FeH(CO)$_2$]$^+$ calcd for $C_{27}H_{40}O_2P_3Fe$, 545.15851; found, 545.15845.

***cis*-[($^{i\mathrm{Pr}}$PP$^{\mathrm{Me}}$P)FeH(CO)$_2$][(ClCH$_2$CO$_2$)(ClCH$_2$CO$_2$H)$_2$] (3) Generated In Situ.** In a glovebox, to a J. Young NMR tube were added **1** (5.0 mg, 0.0092 mmol), chloroacetic acid (3.0 mg, 0.032 mmol), and ∼0.5 mL of C_6D_6. The resulting solution was studied by NMR spectroscopy. The protonation experiment was repeated in a scintillation vial using a minimum amount of toluene, which was, in turn, layered with pentane and kept in a −30 °C freezer. The resulting colorless blade-shaped crystals (obtained within a week) were analyzed by X-ray crystallography and IR spectroscopy. ^{1}H NMR (400 MHz, C_6D_6): δ 8.75 (t, J = 8.0 Hz, Ar*H*, 2H), 7.91 (t, J = 7.6 Hz, Ar*H*, 2H), 7.50 (t, J = 7.6 Hz, Ar*H*, 2H), 7.43−7.32 (m, Ar*H*, 2H), 4.04 (s, ClCH$_2$, 7H), 2.54−2.35 [m, C*H*(CH$_3$)$_2$, 2H], 2.31−2.16 [m, C*H*(CH$_3$)$_2$, 2H], 1.85 (d, $^2J_{H-P}$ = 9.2 Hz, PC*H*$_3$, 3H), 1.10−1.00 [m, CH(C*H*$_3$)$_2$, 6H], 1.00−0.90 [m, CH(C*H*$_3$)$_2$, 6H], 0.81−0.65 [m, CH(C*H*$_3$)$_2$, 6H], 0.62−0.47 [m, CH(C*H*$_3$)$_2$, 6H], −11.43 (td, $^2J_{H-P}$ = 49.6 and 44.0 Hz, Fe*H*, 1H). ^{31}P{^{1}H} NMR (162 MHz, C_6D_6): δ 108.2 (d, $^2J_{P-P}$ = 30.8 Hz, P^{i}Pr$_2$, 2P), 96.0 (t, $^2J_{P-P}$ = 30.8 Hz, *P*Me, 1P). Selected ATR-IR data (solid, cm^{-1}): 2003 ($\nu_{C\equiv O}$), 1959 ($\nu_{C\equiv O}$), 1893 (ν_{Fe-H}).

Synthesis of *cis*-[($^{i\mathrm{Pr}}$PP$^{\mathrm{Me}}$P)FeH(CO)$_2$]BPh$_4$ (4). In a glovebox, to an oven-dried 50 mL Schlenk flask were added **1** (50 mg, 0.092 mmol) and ethanol (5 mL). The flask was removed from the glovebox and connected to a Schlenk line. Formic acid (4.0 μL, 0.11 mmol) was added with continuous stirring under argon. After 15 min, NaBPh$_4$ (36 mg, 0.11 mmol, predissolved in 5 mL of ethanol) was added to the reaction mixture, forming a white precipitate. The suspension was stirred for an additional 1 h and then filtered via cannula. The solid was collected, washed with ethanol (5 × 2 mL), and dried under vacuum to afford the desired product as a white powder (47 mg, 59% yield). X-ray-quality crystals were grown from an ethanol/toluene solution kept at −30 °C. ^{1}H NMR (400 MHz, CD_2Cl_2): δ 8.22 (t, J = 7.6 Hz, Ar*H*, 2H), 7.81−7.67 (m, Ar*H*, 6H), 7.38−7.30 (m, Ar*H* of BPh$_4$, 8H), 7.03 (t, J = 7.2 Hz, Ar*H* of BPh$_4$, 8H), 6.88 (t, J = 7.2 Hz, Ar*H* of BPh$_4$, 4H), 2.90−2.73 [m, C*H*(CH$_3$)$_2$, 4H], 1.87 (d, $^2J_{H-P}$ = 9.2 Hz, PC*H*$_3$, 3H), 1.47−1.37 [m, CH(C*H*$_3$)$_2$, 6H], 1.31−1.15 [m, CH(C*H*$_3$)$_2$, 12H], 0.97−0.86 [m, CH(C*H*$_3$)$_2$, 6H], −11.26 (td, $^2J_{H-P}$ = 49.2 and 45.2 Hz, Fe*H*, 1H). ^{13}C{^{1}H} NMR (101 MHz, CD_2Cl_2): δ 212.6 (dt, $^2J_{C-P}$ = 29.7 and 20.2 Hz, *C*O), 212.2 (dt, $^2J_{C-P}$ = 21.8 and 7.6 Hz, *C*O), 164.5 (q, $^1J_{C-B11}$ = 49.6 Hz; sept, $^1J_{C-B10}$ = 17.2 Hz, C_{ipso} of BPh$_4$), 143.3 (dt, J = 54.0 and 16.7 Hz, Ar*C* bonded to P), 141.4 (ddd, J = 36.7, 24.1, and 21.7 Hz, Ar*C* bonded to P), 136.4 (q, J_{C-B} = 1.5 Hz, Ar*C* of BPh$_4$), 133.2−133.0 (m, Ar*C*), 130.8−130.4 (m, Ar*C*), 126.0 (q, J_{C-B} = 2.7 Hz, Ar*C* of BPh$_4$), 122.1 (s, Ar*C* of BPh$_4$), 31.0 [t, J_{C-P} = 10.0 Hz, *C*H(CH$_3$)$_2$], 30.9 [td, J_{C-P} = 16.6 and 2.6 Hz, *C*H(CH$_3$)$_2$], 22.5 (d, $^1J_{C-P}$ = 31.8 Hz, PCH$_3$), 19.5 [s, CH(*C*H$_3$)$_2$], 18.81 [s, CH(*C*H$_3$)$_2$], 18.79 [t, J_{C-P} = 2.2 Hz, CH(*C*H$_3$)$_2$], 18.5 [s, CH(*C*H$_3$)$_2$]. ^{31}P{^{1}H} NMR (162 MHz, CD_2Cl_2): δ 108.5 (d, $^2J_{P-P}$ = 32.1 Hz, P^{i}Pr$_2$, 2P), 95.7 (t, $^2J_{P-P}$ = 32.1 Hz, *P*Me, 1P). Selected ATR-IR data (solid, cm^{-1}): 2003 ($\nu_{C\equiv O}$), 1971 ($\nu_{C\equiv O}$), 1906 (ν_{Fe-H}). Anal. Calcd for $C_{51}H_{60}O_2P_3BFe$: C, 70.85; H, 6.99. Found: C, 70.27; H, 7.02. ESI-MS of **3** dissolved in MeOH (m/z): [($^{i\mathrm{Pr}}$PP$^{\mathrm{Me}}$P)FeH(CO)$_2$]$^+$ calcd for $C_{27}H_{40}O_2P_3Fe$, 545.15851; found, 545.15852; [BPh$_4$]$^-$ calcd for $C_{24}H_{20}B$, 319.16635; found, 319.16633.

Fe(OCHO)$_2$ Solvated by 1,4-Dioxane. In a glovebox, to an oven-dried 10 mL Schlenk tube were added Fe(OCHO)$_2$·2H$_2$O (100 mg, 0.55 mmol) and 1,4-dioxane (1 mL), giving a pale green suspension. The tube was sealed with a rubber septum, removed from the glovebox, and immersed in an oil bath preheated to 80 °C, after which formic acid (0.20 mL, 5.3 mmol) was added by using a microliter syringe. The mixture was stirred at 80 °C for 18 h. The resulting precipitate was collected by filtration and dried under a vacuum to yield the desired product as a white powder (87 mg, 94% yield). Selected ATR-IR data (solid, cm^{-1}): 1580 (ν_{OCO}), 1400 (δ_{CH}), 1324 (ν_{OCO}), 779 (δ_{OCO}). Anal. Calcd for $C_2H_2O_4Fe\cdot{}^1/_4C_4H_8O_2$: C, 21.46; H, 2.40. Found: C, 21.71; H, 2.42.

Synthesis of ($^{i\mathrm{Pr}}$PP$^{\mathrm{H}}$P)Fe(CO)$_2$ (5). In a glovebox, to an oven-dried 50 mL Schlenk flask were added $^{i\mathrm{Pr}}$PP$^{\mathrm{H}}$P (50 mg, 0.12 mmol), Fe(CO)$_5$ (16 μL, 0.12 mmol), and acetone (5 mL). The flask was removed from the glovebox, connected to a Schlenk line, and subjected to UV radiation using an array of four 368 nm UV LEDs (caution: UV light safety glasses should be worn). After UV irradiation for 20 min, the volatiles were removed under vacuum. The resulting sticky residue was washed with cold pentane (0 °C, 2 mL), dissolved in toluene/pentane, and allowed to crystallize at −30 °C. After 1 month, dark red crystals were obtained. Drying the crystals under a vacuum provided an analytically pure sample (21 mg, 33% yield). X-ray-quality crystals were grown from a toluene/pentane solution kept at −30 °C. ^{1}H NMR (400 MHz, C_6D_6): δ 7.72 (t, J = 6.6 Hz, Ar*H*, 2H), 7.38−7.30 (m, Ar*H*, 2H), 7.10−6.99 (m, Ar*H*, 4H), 6.87 (d, $^1J_{H-P}$ = 336.8 Hz, 1H), 2.59−2.47 [m, C*H*(CH$_3$)$_2$, 2H], 2.46−2.34 [m, C*H*(CH$_3$)$_2$, 2H], 1.48−1.36 [m, CH(C*H*$_3$)$_2$, 6H], 1.16−1.05 [m, CH(C*H*$_3$)$_2$, 6H], 0.95−0.80 [m, CH(C*H*$_3$)$_2$, 12H]. ^{13}C{^{1}H} NMR (101 MHz, C_6D_6): δ 232.4 (td, $^2J_{C-P}$ = 29.8 and 25.1 Hz, *C*O), 221.8 (dt, $^2J_{C-P}$ = 18.5 and 9.3 Hz, *C*O), 147.6

https://doi.org/10.1021/acs.inorgchem.3c03125
Inorg. Chem. 2023, 62, 18714−18723

(ddd, J = 48.7, 16.5, and 13.9 Hz, ArC bonded to P), 144.3 (dt, J = 43.3 and 24.6 Hz, ArC bonded to P), 130.0 (t, J = 7.4 Hz, ArC), 129.4−129.1 (m, ArC), 128.8 (d, J = 18.9 Hz, ArC), 32.5 [t, J = 12.8 Hz, $CH(CH_3)_2$], 30.2 [t, J = 9.1 Hz, $CH(CH_3)_2$], 19.3−19.1 [m, $CH(CH_3)_2$], 18.3 [s, $CH(CH_3)_2$]. $^{31}P\{^1H\}$ NMR (162 MHz, C_6D_6): δ 117.5 (d, $^2J_{P-P}$ = 69.0 Hz, P^iPr_2, 2P), 84.1 (t, $^2J_{P-P}$ = 69.0 Hz, PMe, 1P). Selected ATR-IR data (solid, cm^{-1}): 2266 (ν_{P-H}), 1896 ($\nu_{C\equiv O}$), 1839 ($\nu_{C\equiv O}$). Anal. Calcd for $C_{26}H_{37}O_2P_3Fe$: C, 58.88; H, 7.03. Found: C, 58.30; H, 7.19.

Catalytic Dehydrogenation of Formic Acid. In a glovebox, an oven-dried 10 mL Schlenk tube equipped with a stir bar was loaded with an iron catalyst (2.65 μmol, 0.1 mol % loading) and 1,4-dioxane (0.5 mL) and then sealed with a rubber septum. The tube was removed from the glovebox and attached to a Chemglass gas evolution measurement apparatus (catalog no. CG-1818) filled with mineral oil. Formic acid (100 μL, 2.65 mmol) was added via a microliter syringe, and the tube was quickly immersed in a preheated oil bath. The volume of the produced gas was first measured from a change in the oil level and then corrected by subtracting out the volume obtained from a blank reaction (without a catalyst). TOF and TON were calculated on the basis of a method that was previously described in the literature.[8b,9a,27]

X-ray Structure Determinations. Crystal data collection and refinement parameters are listed in the Supporting Information. The intensity data were collected at 150 K on a Bruker D8 Venture Photon-II diffractometer using Mo Kα radiation (λ = 0.71073 Å). The data frames were processed using SAINT. The data were corrected for decay, Lorentz, and polarization effects, as well as absorption and beam corrections. The structures were determined by a combination of direct methods and the difference Fourier technique as implemented in the SHELX suite of programs and refined by full-matrix least squares on F^2 for reflections out to 0.75 Å. Non-hydrogen atoms were refined with anisotropic displacement parameters. Hydrogen atoms bound to iron, phosphorus, and oxygen were located directly from the difference map, and their coordinates and isotropic displacement parameters were refined. All remaining hydrogen atoms were calculated and treated with a riding model. The isotropic displacement parameters were defined as a^*U_{eq} (a values of 1.5 for methyl and 1.2 for all others) of the adjacent atom. Compound **4** crystallizes as a toluene solvate; the toluene is disordered over an inversion center. One isopropyl group shows disorder in a methyl group, C23/C23B, which was refined with a two-component model (major component occupancy of 74%). Compound **5** crystallizes with three independent molecules in the lattice. Crystal structures of **1**, **3**, **4**·$^1/_2C_7H_8$, and **5** were deposited at the Cambridge Crystallographic Data Centre (CCDC) and assigned the deposition numbers CCDC 2293050−2293053.

■ ASSOCIATED CONTENT

Supporting Information

The Supporting Information is available free of charge at https://pubs.acs.org/doi/10.1021/acs.inorgchem.3c03125.

NMR, IR, and ESI-MS spectra of the iron complexes and more detailed X-ray crystallographic information (PDF)

Accession Codes

CCDC 2293050−2293053 contain the supplementary crystallographic data for this paper. These data can be obtained free of charge via www.ccdc.cam.ac.uk/data_request/cif, or by emailing data_request@ccdc.cam.ac.uk, or by contacting The Cambridge Crystallographic Data Centre, 12 Union Road, Cambridge CB2 1EZ, UK; fax: +44 1223 336033.

■ AUTHOR INFORMATION

Corresponding Author

Hairong Guan − *Department of Chemistry, University of Cincinnati, Cincinnati, Ohio 45221-0172, United States;* orcid.org/0000-0002-4858-3159; Email: hairong.guan@uc.edu

Authors

Bedraj Pandey − *Department of Chemistry, University of Cincinnati, Cincinnati, Ohio 45221-0172, United States*

Jeanette A. Krause − *Department of Chemistry, University of Cincinnati, Cincinnati, Ohio 45221-0172, United States*

Complete contact information is available at: https://pubs.acs.org/10.1021/acs.inorgchem.3c03125

Notes

The authors declare no competing financial interest.

■ ACKNOWLEDGMENTS

The authors thank the National Science Foundation (NSF) Chemical Catalysis Program for support of this research project (CHE-2102192) and the NSF MRI Program for support of the instrumentation used in this study, which includes a Bruker D8 Venture diffractometer (CHE-1625737) and a Bruker NEO400 MHz NMR spectrometer (CHE-1726092). B.P. thanks the University of Cincinnati for a Doctoral Enhancement Research Fellowship. The authors are also grateful to Dr. Larry Sallans (University of Cincinnati) for his assistance with mass spectral analysis.

■ REFERENCES

(1) Bullock, R. M.; Chen, J. G.; Gagliardi, L.; Chirik, P. J.; Farha, O. K.; Hendon, C. H.; Jones, C. W.; Keith, J. A.; Klosin, J.; Minteer, S. D.; Morris, R. H.; Radosevich, A. T.; Rauchfuss, T. B.; Strotman, N. A.; Vojvodic, A.; Ward, T. R.; Yang, J. Y.; Surendranath, Y. Using Nature's Blueprint to Expand Catalysis with Earth-Abundant Metals. *Science* **2020**, *369*, No. eabc3183.

(2) Schlaf, M.; Ghosh, P.; Fagan, P. J.; Hauptman, E.; Bullock, R. M. Metal-Catalyzed Selective Deoxygenation of Diols to Alcohols. *Angew. Chem., Int. Ed.* **2001**, *40*, 3887−3890.

(3) Korstanje, T. J.; van der Vlugt, J. I.; Elsevier, C. J.; de Bruin, B. Hydrogenation of Carboxylic Acids with a Homogeneous Cobalt Catalyst. *Science* **2015**, *350*, 298−302.

(4) (a) Bernskoetter, W. H.; Hazari, N. Reversible Hydrogenation of Carbon Dioxide to Formic Acid and Methanol: Lewis Acid Enhancement of Base Metal Catalysts. *Acc. Chem. Res.* **2017**, *50*, 1049−1058. (b) Guan, C.; Pan, Y.; Zhang, T.; Ajitha, M. J.; Huang, K.-W. An Update on Formic Acid Dehydrogenation by Homogeneous Catalysis. *Chem. - Asian J.* **2020**, *15*, 937−946. (c) Iglesias, M.; Fernández-Alvarez, F. J. Advances in Nonprecious Metal Homogeneously Catalyzed Formic Acid Dehydrogenation. *Catalysts* **2021**, *11*, 1288. (d) Onishi, N.; Kanega, R.; Kawanami, H.; Himeda, Y. Recent Progress in Homogeneous Catalytic Dehydrogenation of Formic Acid. *Molecules* **2022**, *27*, 455.

(5) (a) Mellmann, D.; Sponholz, P.; Junge, H.; Beller, M. Formic Acid as a Hydrogen Storage Material − Development of Homogeneous Catalysts for Selective Hydrogen Release. *Chem. Soc. Rev.* **2016**, *45*, 3954−3988. (b) Eppinger, J.; Huang, K.-W. Formic Acid as a Hydrogen Energy Carrier. *ACS Energy Lett.* **2017**, *2*, 188−195. (c) Sordakis, K.; Tang, C.; Vogt, L. K.; Junge, H.; Dyson, P. J.; Beller, M.; Laurenczy, G. Homogeneous Catalysis for Sustainable Hydrogen Storage in Formic Acid and Alcohols. *Chem. Rev.* **2018**, *118*, 372−433. (d) Onishi, N.; Laurenczy, G.; Beller, M.; Himeda, Y. Recent Progress for Reversible Homogeneous Catalytic Hydrogen Storage in Formic Acid and in Methanol. *Coord. Chem. Rev.* **2018**, *373*, 317−332. (e) Guo, J.; Yin, C. K.; Zhong, D. L.; Wang, Y. L.; Qi, T.; Liu, G. H.; Shen, L. T.; Zhou, Q. S.; Peng, Z. H.; Yao, H.; Li, X. B. Formic Acid as a Potential On-Board Hydrogen Storage Method: Development of Homogeneous Noble Metal Catalysts for Dehydrogenation Reactions. *ChemSusChem* **2021**, *14*, 2655−2681. (f) Dutta, I.; Chatterjee, S.; Cheng, H.; Parsapur, R. K.; Liu, Z.; Li, Z.; Ye, E.; Kawanami, H.; Low, J. S. C.; Lai, Z.; Loh, X. J.; Huang, K.-W. Formic Acid to Power towards Low-Carbon Economy. *Adv. Energy Mater.* **2022**, *12*, 2103799.

(6) Morris, D. J.; Clarkson, G. J.; Wills, M. Insights into Hydrogen Generation from Formic Acid Using Ruthenium Complexes. *Organometallics* **2009**, *28*, 4133−4140.
(7) (a) Boddien, A.; Loges, B.; Gärtner, F.; Torborg, C.; Fumino, K.; Junge, H.; Ludwig, R.; Beller, M. Iron-Catalyzed Hydrogen Production from Formic Acid. *J. Am. Chem. Soc.* **2010**, *132*, 8924−8934. (b) Boddien, A.; Gärtner, F.; Jackstell, R.; Junge, H.; Spannenberg, A.; Baumann, W.; Ludwig, R.; Beller, M. *ortho*-Metalation of Iron(0) Tribenzylphosphine Complexes: Homogeneous Catalysts for the Generation of Hydrogen from Formic Acid. *Angew. Chem., Int. Ed.* **2010**, *49*, 8993−8996.
(8) (a) Zell, T.; Butschke, B.; Ben-David, Y.; Milstein, D. Efficient Hydrogen Liberation from Formic Acid Catalyzed by a Well-Defined Iron Pincer Complexes under Mild Conditions. *Chem. - Eur. J.* **2013**, *19*, 8068−8072. (b) Bielinski, E. A.; Lagaditis, P. O.; Zhang, Y.; Mercado, B. Q.; Würtele, C.; Bernskoetter, W. H.; Hazari, N.; Schneider, S. Lewis Acid-Assisted Formic Acid Dehydrogenation Using a Pincer-Supported Iron Catalyst. *J. Am. Chem. Soc.* **2014**, *136*, 10234−10237. (c) Mellone, I.; Gorgas, N.; Bertini, F.; Peruzzini, M.; Kirchner, K.; Gonsalvi, L. Selective Formic Acid Dehydrogenation Catalyzed by Fe-PNP Pincer Complexes Based on the 2,6-Diaminopyridine Scaffold. *Organometallics* **2016**, *35*, 3344−3349. (d) Curley, J. B.; Smith, N. E.; Bernskoetter, W. H.; Hazari, N.; Mercado, B. Q. Catalytic Formic Acid Dehydrogenation and CO_2 Hydrogenation Using Iron PN^RP Pincer Complexes with Isonitrile Ligands. *Organometallics* **2018**, *37*, 3846−3853. (e) Curley, J. B.; Bernskoetter, W. H.; Hazari, N. Additive-Free Formic Acid Dehydrogenation Using a Pincer-Supported Iron Catalyst. *ChemCatChem.* **2020**, *12*, 1934−1938. (f) Pandey, B.; Krause, J. A.; Guan, H. Iron Dihydride Complex Stabilized by an All-Phosphorus-Based Pincer Ligand and Carbon Monoxide. *Inorg. Chem.* **2022**, *61*, 11143−11155. (g) Pandey, B.; Krause, J. A.; Guan, H. Methyl Effects on the Stereochemistry and Reactivity of PPP-Ligated Iron Hydride Complexes. *Inorg. Chem.* **2023**, *62*, 967−978.
(9) (a) Boddien, A.; Mellmann, D.; Gärtner, F.; Jackstell, R.; Junge, H.; Dyson, P. J.; Laurenczy, G.; Ludwig, R.; Beller, M. Efficient Dehydrogenation of Formic Acid Using an Iron Catalyst. *Science* **2011**, *333*, 1733−1736. (b) Bertini, F.; Mellone, I.; Ienco, A.; Peruzzini, M.; Gonsalvi, L. Iron(II) Complexes of the Linear *rac*-Tetraphos-1 Ligand as Efficient Homogeneous Catalysts for Sodium Bicarbonate Hydrogenation and Formic Acid Dehydrogenation. *ACS Catal.* **2015**, *5*, 1254−1265. (c) Montandon-Clerc, M.; Dalebrook, A. F.; Laurenczy, G. Quantitative Aqueous Phase Formic Acid Dehydrogenation Using Iron(II) Based Catalysts. *J. Catal.* **2016**, *343*, 62−67.
(10) (a) Celaje, J. J. A.; Lu, Z.; Kedzie, E. A.; Terrile, N. J.; Lo, J. N.; Williams, T. J. A Prolific Catalyst for Dehydrogenation of Neat Formic Acid. *Nat. Commun.* **2016**, *7*, 11308. (b) Cohen, S.; Borin, V.; Schapiro, I.; Musa, S.; De-Botton, S.; Belkova, N. V.; Gelman, D. Ir(III)-PC(sp^3)P Bifunctional Catalysts for Production of H_2 by Dehydrogenation of Formic Acid: Experimental and Theoretical Study. *ACS Catal.* **2017**, *7*, 8139−8146. (c) Wang, S.; Huang, H.; Roisnel, T.; Bruneau, C.; Fischmeister, C. Base-Free Dehydrogenation of Aqueous and Neat Formic Acid with Iridium(III) Cp*(dipyridylamine) Catalysts. *ChemSusChem* **2019**, *12*, 179−184. (d) Kar, S.; Rauch, M.; Leitus, G.; Ben-David, Y.; Milstein, D. Highly Efficient Additive-Free Dehydrogenation of Neat Formic Acid. *Nat. Catal.* **2021**, *4*, 193−201.
(11) We have used *cis*-($^{iPr}PP^HP$)Fe(CO)H_2 to catalyze the dehydrogenation of neat formic acid, which resulted in merely 67 turnovers. For details, see ref 8f.
(12) Curley, J. B.; Smith, N. E.; Bernskoetter, W. H.; Ertem, M. Z.; Hazari, N.; Mercado, B. Q.; Townsend, T. M.; Wang, X. Understanding the Reactivity and Decomposition of a Highly Active Iron Pincer Catalyst for Hydrogenation and Dehydrogenation Reactions. *ACS Catal.* **2021**, *11*, 10631−10646.
(13) Fleissner, S.; Pittenauer, E.; Kirchner, K. Electrospray Ionization Tandem Mass Spectrometric Study of Selected Phosphine-Based Ligands for Catalytically Active Organometallics. *J. Am. Soc. Mass Spectrom.* **2023**, *34*, 1647−1652.
(14) Bielinski, E. A.; Förster, M.; Zhang, Y.; Bernskoetter, W. H.; Hazari, N.; Holthausen, M. C. Base-Free Methanol Dehydrogenation Using a Pincer-Supported Iron Compound and Lewis Acid Co-catalyst. *ACS Catal.* **2015**, *5*, 2404−2415.
(15) Koehne, I.; Schmeier, T. J.; Bielinski, E. A.; Pan, C. J.; Lagaditis, P. O.; Bernskoetter, W. H.; Takase, M. K.; Würtele, C.; Hazari, N.; Schneider, S. Synthesis and Structure of Six-Coordinate Iron Borohydride Complexes Supported by PNP Ligands. *Inorg. Chem.* **2014**, *53*, 2133−2143.
(16) Addison, A. W.; Rao, T. N.; Reedijk, J.; van Rijn, J.; Verschoor, G. C. Synthesis, Structure, and Spectroscopic Properties of Copper(II) Compounds Containing Nitrogen−Sulphur Donor Ligands; the Crystal and Molecular Structure of Aqua[1,7-bis(*N*-methylbenzimidazol-2′-yl)-2,6-dithiaheptane]copper(II) Perchlorate. *J. Chem. Soc., Dalton Trans.* **1984**, 1349−1356.
(17) Jayarathne, U.; Hazari, N.; Bernskoetter, W. H. Selective Iron-Catalyzed *N*-Formylation of Amines using Dihydrogen and Carbon Dioxide. *ACS Catal.* **2018**, *8*, 1338−1345.
(18) Trovitch, R. J.; Lobkovsky, E.; Chirik, P. J. Bis(diisopropylphosphino)pyridine Iron Dicarbonyl, Dihydride, and Silyl Hydride Complexes. *Inorg. Chem.* **2006**, *45*, 7252−7260.
(19) (a) Bichler, B.; Holzhacker, C.; Stöger, B.; Puchberger, M.; Veiros, L. F.; Kirchner, K. Heterolytic Cleavage of Dihydrogen by an Iron(II) PNP Pincer Complex via Metal−Ligand Cooperation. *Organometallics* **2013**, *32*, 4114−4121. (b) Glatz, M.; Gorgas, N.; Stöger, B.; Pittenauer, E.; Ferreira, L.; Veiros, L. F.; Calhorda, M. J.; Kirchner, K. Structural and Electronic Properties of Iron(0) PNP Pincer Complexes. *Z. Anorg. Allg. Chem.* **2021**, *647*, 1429−1435.
(20) Viertelhaus, M.; Adler, P.; Clérac, R.; Anson, C. E.; Powell, A. K. Iron(II) Formate $[Fe(O_2CH)_2]$ •1/3HCO_2H: A Mesoporous Magnet − Solvothermal Syntheses and Crystal Structures of the Isomorphous Framework Metal(II) Formates $[M(O_2CH)_2]$•*n*(Solvent) (M = Fe, Co, Ni, Zn, Mg). *Eur. J. Inorg. Chem.* **2005**, *2005*, 692−703.
(21) Golovin, M. N.; Rahman, M. M.; Belmonte, J. E.; Giering, W. P. Quantitative Separation of σ- and π-Components of Transition Metal−Phosphorus Bonding and the Application of Ligand Effects in Organometallic Chemistry. *Organometallics* **1985**, *4*, 1981−1991.
(22) Rhoda, R. N.; Fraioli, A. V.; Taylor, W. L.; Kleinberg, J. Iron(II) Formate. In *Inorganic Syntheses*; Bailar, J. C., Jr., Ed.; McGraw-Hill: New York, 1953; pp 159−161.
(23) Weber, G. Iron(II) Formate Dihydrate. *Acta Crystallogr.* **1980**, *B36*, 3107−3109.
(24) Neary, M. C.; Parkin, G. Nickel-Catalyzed Release of H_2 from Formic Acid and a New Method for the Synthesis of Zerovalent Ni(PMe_3)$_4$. *Dalton Trans.* **2016**, *45*, 14645−14650.
(25) Kim, Y.-E.; Kim, J.; Lee, Y. Formation of a Nickel Carbon Dioxide Adduct and Its Transformation Mediated by a Lewis Acid. *Chem. Commun.* **2014**, *50*, 11458−11461.
(26) Mankad, N. P.; Rivard, E.; Harkins, S. B.; Peters, J. C. Structural Snapshots of a Flexible Cu_2P_2 Core That Accommodates the Oxidation States Cu^ICu^I, $Cu^{1.5}Cu^{1.5}$, and $Cu^{II}Cu^{II}$. *J. Am. Chem. Soc.* **2005**, *127*, 16032−16033.
(27) Lentz, N.; Aloisi, A.; Thuéry, P.; Nicolas, E.; Cantat, T. Additive-Free Formic Acid Dehydrogenation Catalyzed by a Cobalt Complex. *Organometallics* **2021**, *40*, 565−569.

https://doi.org/10.1021/acs.inorgchem.3c03125
Inorg. Chem. 2023, 62, 18714−18723